Article

Turbulent Flow Heat Transfer and Thermal Stress Improvement of Gas Turbine Blade Trailing Edge Cooling with Diamond-Type TPMS Structure

Kirttayoth Yeranee [ID], Yu Rao *, Chao Xu, Yueliang Zhang [ID] and Xiyuan Su

Institute of Turbomachinery, School of Mechanical Engineering, Shanghai Jiao Tong University, Shanghai 200240, China; krittayoch.y@gmail.com (K.Y.); chao_xu@sjtu.edu.cn (C.X.); zhangyueliang@sjtu.edu.cn (Y.Z.); sxy12138@sjtu.edu.cn (X.S.)
* Correspondence: yurao@sjtu.edu.cn

Abstract: Additive manufacturing allows the fabrication of relatively complex cooling structures, such as triply periodic minimal surface (TPMS), which offers high heat transfer per unit volume. This study shows the turbulent flow heat transfer and thermal stress of the Diamond-TPMS topology in the gas turbine blade trailing edge channel. The thermal-fluid-solid analysis of the Diamond-TPMS structure, made of directionally solidified GTD111, at the nearly realistic gas turbine condition is executed, and the results are compared with the conventional pin fin array at the Reynolds number of 30,000. Compared to the baseline pin fin structure, the Diamond-TPMS model distributes flow characteristics more uniformly throughout the channel. The overall heat transfer enhancement, friction factor ratio, and thermal performance are increased by 145.3%, 200.9%, and 32.5%, respectively. The temperature, displacement, and thermal stress in the Diamond-TPMS model are also distributed more evenly. The average temperature on the external surface in the Diamond-TPMS model is lower than the baseline pin fin array by 19.9%. The Diamond-TPMS network in the wedge-shaped cooling channel helps reduce the volume displacement due to the material thermal expansion by 29.3%. Moreover, the volume-averaged von Mises stress in the Diamond-TPMS structure is decreased by 28.8%.

Keywords: diamond structure; gas turbine blade; heat transfer; thermal stress; trailing edge; turbulent flow

1. Introduction

Gas turbine engines are widely used in aviation propulsion and land-based power plants. High power density, high thermal efficiency, and superior performance are among the advantages compared to other power generations. Performance improvements of gas turbine engines are motivated by the purpose of decreasing fuel consumption, saving subsequent expenses, and reducing carbon dioxide (CO_2) emissions, which are the primary cause of global warming. Therefore, researchers and designers have intensively and extensively developed gas turbine performance.

Increasing the turbine inlet temperature (TIT) has been the most effective way to improve gas turbine power and efficiency in the last 50 years. With substantial elevations, gas turbine engine operating temperatures have consistently elevated over the past decades. The TIT of fourth-generation aero-engines has attained between 1800 and 2000 K. It has been observed the combined cycle plant with around 2000 K has reached an efficiency of approximately 65% [1]. The fifth-generation TIT of an aero-engine will achieve 2100 to 2250 K. Mitsubishi Company shows Japan's M701J heavy-duty gas turbines with the TIT of approximately 1900 K. Furthermore, the advanced heavy-duty gas turbine operating temperature will move forward to 2000 K.

Many recent studies also focused on using alternative materials for the gas turbine blade to prevent the blade losing structure from high temperatures [2]. Nekahi et al. [3]

compared the stator blade material made of ceramic groups, i.e., Hafnium diboride (HfB_2), Zirconium diboride (ZrB_2), and Titanium diboride (TiB_2). They observed all these materials could withstand high temperatures and applied compressive stresses. They also showed the HfB_2 bore more thermal stress than the others. Sadegh et al. [4] compared the temperature distribution, displacement, and thermal stress of a stator turbine blade made of ZrB_2 and M152. It was found the ZrB_2 outperformed the M152 in terms of temperature distribution and displacement; also, the thermal stress was higher. Abid and Sarowar [5] compared superalloys and ceramic materials, i.e., Inconel 718, grade 5 titanium (Ti-6Al-4V), Nimonic 80A, Niobium diboride (NbB_2), and directionally solidified superalloy (GTD111 DS) in gas turbine stator blade under operating conditions. It was concluded Ti-6Al-4V was the most suitable material for manufacturing gas turbine stator blades.

Although superalloys/ceramics and manufacturing processes have allowed gas turbine blades to withstand below 1300 K [6], the temperatures generated by the combustor would soon exceed 2250 K. In addition, it has been reported the maximum temperature for the superalloy was only 8 K per year, whereas the TIT increased up to a rate of 20 K per year [7]. Therefore, to close the gap between the temperature limit of the blade materials and the maximum temperatures from the combustor, advanced cooling methods must be implemented to cool the blades, thus preventing thermal failure at extremely high operating temperatures.

Different cooling methods are used in different sections of a gas turbine blade, including external and internal cooling, to cool down the blade, as shown in Figure 1 [8]. Film cooling holes at the body, platform, tip, and trailing edge are the ways to release the air to cool the external blade. On the other hand, internal cooling, used to cool the blade from the inside, comprises three main parts based on the heat transfer required: the leading edge, the middle portion, and the trailing edge. The internal cooling strategies of modern gas turbines include jet impingement, rib turbulators, and pin fin, dimple/protrusion, latticework, etc.
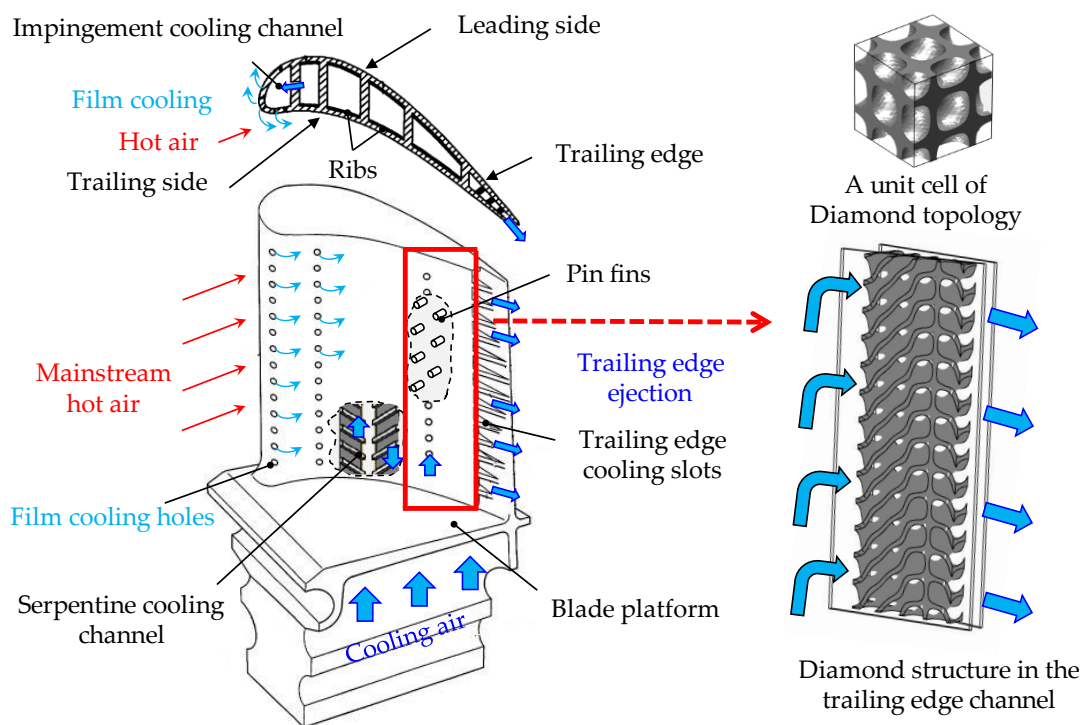
Figure 1. Sketch of a modern gas turbine blade [8]; also shown is the Diamond-type TPMS structure design for the trailing edge cooling channel.

Most of the prior research indicates the trailing edge region suffers a higher temperature than other sections, and the narrow geometry of this region is the primary cause of the high-temperature distribution [9]. Pin fin elements are commonly used in trailing edge internal cooling, providing additional maintenance in this region. The impingement flow enhances high heat transfer on the pin elements. Additionally, regions of high mixing are generated adjacent to the pin fins. These flow patterns disturb the flow boundary layer and induce high turbulence, thereby enhancing endwall heat transfer. The pin fin shape and arrangement obviously affect the thermal performance.

Recently, due to the rapid development of the advanced manufacturing method, i.e., additive manufacturing (AM), many turbine blade designers have focused on enhancing cooling performance in the channels using different complex structures, such as lattice-frame materials [10,11]. Kaur and Singh [12] printed different strut-based lattice structures using resin and detailed the endwall heat transfer characteristics. They found the averaged endwall heat transfer of the octahedron family lattice structures was increased by 2.96–3.05 times compared to the smooth channel. Kaur [13] observed the Cube structure provided the best thermal performance value compared to Octet, Tetrakaidecahedron (TKD), and face diagonal-cube models. Shen et al. [14] revealed the Kagome structures in a wedge-shaped channel decreased the recirculation flow at the tip region and enhanced endwall heat transfer with slightly increased pressure loss to the conventional pin fin array.

Many researchers have recently focused on the cellular lattice network, also known as triply periodic minimal surfaces (TPMS), with compact and significant thermal properties. The TPMS networks are self-supporting structures, and several studies have confirmed their mechanical capabilities were better than the conventional pin fin or strut-based lattice structures. The TPMS-based structures, such as Diamond and Gyroid, have a high heat transfer rate per unit volume, outperforming the lattice-frame material in a cooling channel [15]. Kaur et al. [16] showed the Gyroid structure enhanced heat transfer better than the TKD because of the larger wetted area. Khalil et al. [17] observed the solid-based Gyroid and Diamond designs showed lower flow resistance than the X-type structure. Zheng [18] reported the solid-based Gyroid, Diamond, and Primitive structures enhanced heat transfer performance higher than the Kagome core due to smoother surfaces and larger wetted areas.

The TPMS-based structures have been used to improve the flow and heat transfer of gas turbine blade trailing edge channel. Yeranee and Rao [19] inserted different Gyroid designs in a wedge-shaped cooling channel, replacing the conventional pin fin array. They found all Gyroid designs improved cooling uniformity and increased the thermal performance by up to 75.6%, superior to the circular pin fin array. Later, Yeranee and Rao [20] found the sheet-based Diamond structure showed the highest thermal performance among different TPMS topologies, by about 77.3%, compared to the conventional pin fin array. The heat transfer distribution was also more uniform, particularly at the channel outlet. Yeranee et al. [21] confirmed the Diamond-TPMS network provided uniform flow distributions and reduced the heat transfer differences between the leading and trailing walls under rotating conditions. Therefore, it can be concluded with the high heat transfer and flow uniformity of the Diamond-TPMS structure, the turbine blades' durability can be extended.

The previous research rarely found the temperature distribution, displacement, and thermal stress of the TPMS-based structures in the turbine blade. The thermal stress occurring at unusually high temperatures is one of the major issues during gas turbine operation. The thermal stress causes the turbine blades' failure due to the creeping fatigue effect. The surface micro-cracks are developed due to the slip of boundary grains (large displacement), and the blade cracks due to large amounts of stress. Alkebsi et al. [22] compared the optimized model's weight, stress, and deformation with three TPMS topologies, i.e., Gyroid, Diamond, and Primitive, in the gas turbine blades. They found the TPMS-based structures in the blade could reduce the weight by up to 40.3%, decrease the stress by 25.5%, and show

less deformation by 19.6% compared to the original turbine blade. However, the cooling performance that influenced the thermal expansion was not considered.

Therefore, in this research, the thermo-fluid-solid coupling investigation is executed on the heat transfer and thermal stress of the trailing edge channel with the optimal TPMS-based structure (Diamond topology). The Diamond-TPMS structure is selected in this investigation because it shows uniform flow and heat transfer distributions, even though the mechanical behaviors are similar to other TPMS networks, as found in many previous studies [23–25]. The material and boundary conditions are set based on the nearly actual gas turbine operating conditions. The results are compared with the conventional pin fin array.

2. Methodology

2.1. Wedge-Shaped Model

Based on the geometrical configurations of the trailing edge of the gas turbine blade, the numerical model is designed as a wedge-shaped channel equipped with the pin fin and Diamond structures, as depicted in Figure 2. The dimensions of the wedge-shaped model in this research corresponded to the experimental wedge-shaped model examined by Liang et al. [26], including the fluid and solid domains. The fluid domain comprises an inlet, a turning region, a channel in a wedged shape, and an outlet. The inlet hydraulic diameter (D_h) is 33.9 mm. The length in the radial and lateral directions is 179 mm and 100 mm, respectively. The angle of the wedge-shaped channel is 15 deg. A row of horseshoe pin fin structures is placed at the outlet upstream. The length of the channel outlet is 150 mm to prevent backflow and ensure numerical stability [19–21].
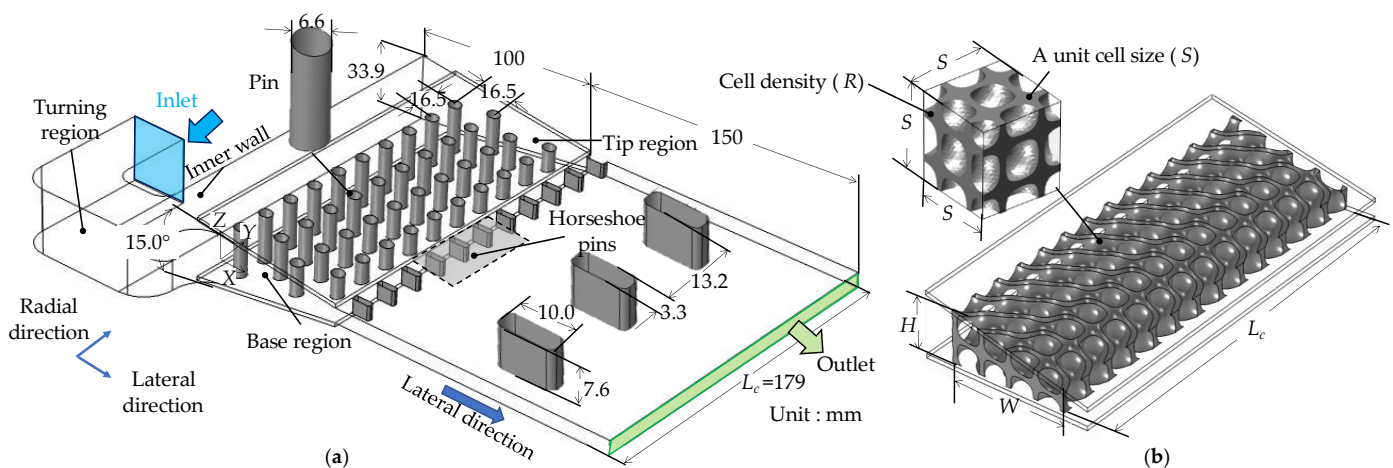
Figure 2. Wedge-shaped channel equipped with (**a**) baseline pin fin structure (**b**) Diamond network.

Pin fin array and Diamond structure are inserted under thin plates for the solid domain. Four-column circular pin fins are arranged in the lateral direction, and each column contains ten pin fin structures, as seen in Figure 2a. The diameter of the pin fin is 6.6 mm. The pin fin array is arranged in a staggered configuration with lateral and radial distances of 16.5 mm. The second model is the trailing edge channel filled with the Diamond structure, as shown in Figure 2b. In this model, the pin fin arrays are replaced by the Diamond network, and the Diamond structure is generated by MSLattice software [27]. The height (H), width (W), length (L_c), and unit size (S) of the Diamond cell are 27, 56.1, 176, and 27 mm. The Diamond density (R) is 30%. The smallest thickness of the Diamond designs in this numerical model is about 1.5 mm. Hence, this small thickness of about 0.5 mm could be successfully printed using the powder-based fusion method (PBF) [15], as this numerical model is scaled up by a factor of 3 of an actual gas turbine blade [26].

2.2. Governing Equations

To ensure the safe and efficient operation of the gas turbine, large deformation of the blade is not allowed during the working process. Generally, the convection heat transfer mechanism transfers high temperature from the continuous hot gases to the blade. The fixed supports of the blade, together with the temperature gradient around the cooling channels, cause volumetric expansion and subsequent thermal stresses. In the present work, the thermomechanical behavior of blades is investigated by the following governing equations, i.e., continuity, Navier–Stokes, heat diffusion, and linear elastic equations.

The compressible and steady-state flow is considered in this simulation; hence, the continuity and Navier–Stokes equations can be written as follows:

$$\rho \nabla \cdot \boldsymbol{u} = 0 \tag{1}$$

$$\rho (\nabla \cdot \boldsymbol{u})\boldsymbol{u} = \nabla \cdot \left[-p\boldsymbol{I} + (\mu + \mu_T)\left(\nabla \boldsymbol{u} + (\nabla \boldsymbol{u})^*\right) - \frac{2}{3}(\mu + \mu_T)(\nabla \cdot \boldsymbol{u})\boldsymbol{I} - \frac{2}{3}\rho k_f \boldsymbol{I} \right] \tag{2}$$

where ρ is the fluid density. $\boldsymbol{u}$ indicates the fluid velocity vector. ∇ signifies the gradient operator. p denotes the pressure field. $\boldsymbol{I}$ is the identical tensor. μ represents the fluid dynamic viscosity, while μ_T is the turbulent dynamic viscosity. * represents the transpose, and k_f is the fluid thermal conductivity.

The thermal convection-diffusion equation in the fluid domain is written as follows:

$$\rho c_f \boldsymbol{u} \nabla T = \nabla \cdot \left(k_f \nabla T \right) \tag{3}$$

where c_f is the fluid heat capacity.

The energy equation in the solid domain is expressed as follows:

$$-\nabla \cdot (k_s \nabla T) = 0 \tag{4}$$

where k_s is the solid thermal conductivity.

The solution of the above equations provides the temperature distribution on the blade. Then, the linear elastic material governing equation is described as follows:

$$\nabla \cdot \sigma_C + \boldsymbol{F}_b = 0 \tag{5}$$

where σ_C is the Cauchy stress tensor, and $\boldsymbol{F}_b$ means the body force per unit volume in the solid domain.

To concise this section, the linear elastic material equation details can be observed in Refs. [3,4]. Here, the von Mises stress (σ_V) that can be calculated based on the Cauchy stress tensor ($\sigma_{C,i}$) and shear stress (τ_{ij}) is given as follows:

$$\sigma_V = \sqrt{\frac{(\sigma_{C,X} - \sigma_{C,Y})^2 + (\sigma_{C,Z} - \sigma_{C,Y})^2 + (\sigma_{C,X} - \sigma_{C,Z})^2 + 6\left(\tau_{XY}^2 + \tau_{XZ}^2 + \tau_{ZY}^2\right)}{2}} \tag{6}$$

The continuity, Navier–Stokes, heat diffusion, and linear elastic equations in this analysis are solved using the finite element method (FEM) via COMSOL Multiphysics 5.5 [3–5]. The fluid flow in the module "Turbulent Flow" and heat transfer in "Heat Transfer in Solids and Fluids" are coupled using "Non-isothermal Flow". Then, the heat transfer in "Heat Transfer in Solids and Fluids" and the structure in the module "Solid Mechanics" are coupled by "Thermal Expansion".

2.3. Material Properties

The temperature-dependent properties of air are employed. Besides, the alloy with high tensile strength (directionally solidified nickel-based GTD111, known as "GTD111 DS") is used for the solid domain as it is widely adopted in rotating compo-

nents subjected to extreme high-temperature operating. Here, the air density is defined through the ideal gas law, assuming adiabatic behavior as follows:

$$\rho = \frac{M_n p_{Amb}}{R_{con} T} \tag{7}$$

where R_{con} is the gas constant, the built-in constant in COMSOL Multiphysics. M_n is the molar mass, which equals 0.02897 kg/mol. p_{Amb} is the ambient air. The ratio of specific heat is 1.4. The air properties, including thermal conductivity (k_f), heat capacity (c_f), and dynamic viscosity (μ), are expressed as follows [28]:

$$k_f = -2.276 \times 10^{-3} + 1.154 \times 10^{-4}T - 7.903 \times 10^{-8}T^2 + 4.117 \times 10^{-11}T^3 - 7.439 \times 10^{-15}T^4 \tag{8}$$

$$c_f = 1047.64 - 3.726 \times 10^{-1}T + 9.453 \times 10^{-4}T^2 - 6.024 \times 10^{-7}T^3 + 1.286 \times 10^{-10}T^4 \tag{9}$$

$$\mu = -8.383 \times 10^{-7} + 8.357 \times 10^{-7}T - 7.694 \times 10^{-11}T^2 + 4.644 \times 10^{-14}T^3 - 1.066 \times 10^{-17}T^4 \tag{10}$$

The temperature-dependent properties of the alloy, involving the density (ρ_s), thermal conductivity (k_s), and heat capacity (c_s), are shown as follows:

$$\rho_s = 8375.7 - 2.799 \times 10^{-1}T + 6.631 \times 10^{-5}T^2 - 3.116 \times 10^{-7}T^3 + 3.316 \times 10^{-10}T^4 - 1.286 \times 10^{-13}T^5 \tag{11}$$

$$k_s = 1.673 + 3.576 \times 10^{-2}T - 5.558 \times 10^{-5}T^2 + 5.532 \times 10^{-8}T^3 - 2.026 \times 10^{-11}T^4 \tag{12}$$

$$c_s = 323.7 + 4.579 \times 10^{-1}T - 4.394 \times 10^{-4}T^2 + 2.208 \times 10^{-7}T^3 - 4.459 \times 10^{-11}T^4 \tag{13}$$

The reference temperature in the linear elastic material equation is 300 K, and Poisson's ratio is fixed at 0.33 to ease the calculation [29]. Moreover, the material is isotropic, and any coating is neglected. Young's modulus (E_s) and coefficient of thermal expansion (α_s) depending upon the temperature are given as follows:

$$E_s = 1.273 \times 10^{11} - 2.0386 \times 10^7 T + 15877.53T^2 - 21.027T^3 \tag{14}$$

$$\alpha_s = -3.319 \times 10^{-3} + 1.153 \times 10^{-5}T - 3.922 \times 10^{-9}T^2 + 1.506 \times 10^{-11}T^3 - 1.53 \times 10^{-14}T^4 + 5.8 \times 10^{-18}T^5 \tag{15}$$

2.4. Boundary Conditions

Figure 3 depicts the boundary conditions of the fluid and solid domains to analyze the flow, heat transfer, and thermal stress of the trailing edge equipped with the circular pin fin and Diamond structures. The flow and heat transfer boundary conditions are the same as those used for the internal cooling channel of the gas turbine blade trailing edge in the previous studies [19,20]. At the inlet boundary, a fully developed flow at Reynolds number of 30,000 with an inlet temperature of T_{in} = 600 K is specified. The Reynolds number is calculated by $Re = \rho U_{in} D_h / \mu$; U_{in} is the inlet velocity. At the outlet boundary, the gauge pressure of zero is imposed. The top and bottom boundaries of the thin plates are treated with a uniform heat flux of $q_0 = 90{,}000$ W/m^2. The uniform heat flux is used instead of high-velocity hot gas because the temperature changes are minor when considering only the trailing edge region. The no-slip conditions are specified on the remaining surfaces.

The solution of the linear elastic equation requires related solid mechanics boundary conditions. As the gas turbine blade trailing edge is only considered in this study, the boundary conditions are simplified from the previous investigations where the full gas turbine blade is considered [3,4]. Here, the fixed constraint boundary condition (displacement vector = 0) is applied on four surfaces to mimic the gas turbine blade trailing edge, as shown in Figure 3b [30]. Finally, all other boundaries on the solid domain are specified as a free boundary condition to allow the blade to deform freely due to thermal expansion.
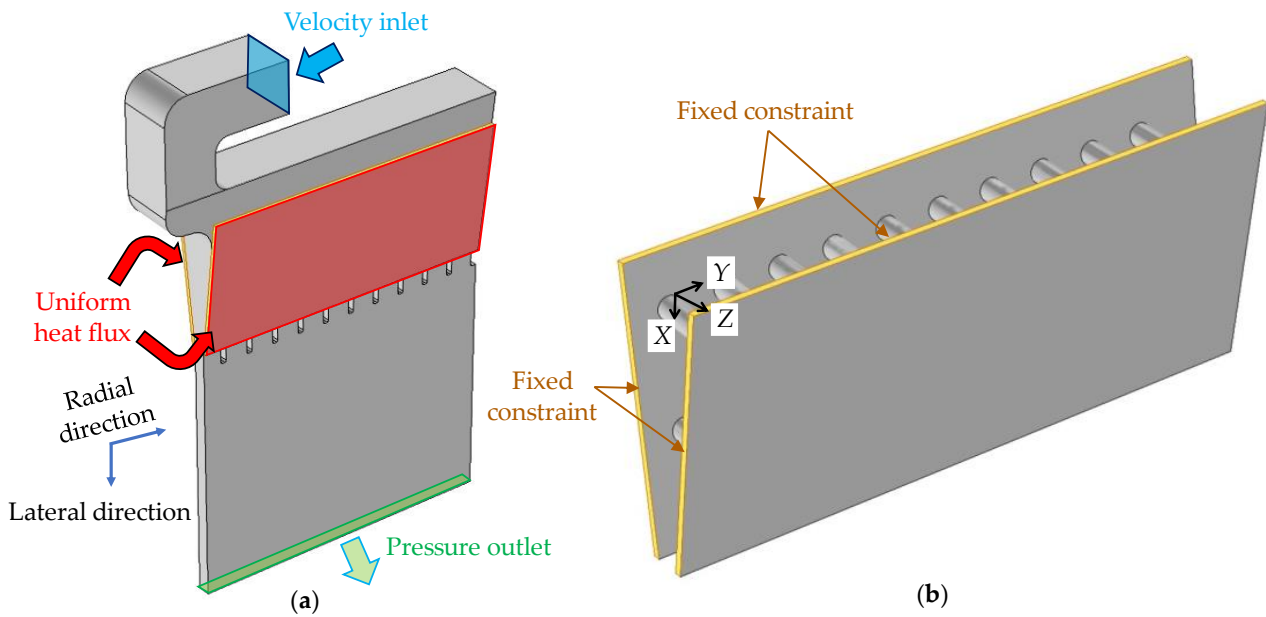
Figure 3. Boundary condition: (**a**) boundary conditions for turbulent flow and heat transfer modules and (**b**) for solid mechanics modules.

2.5. Numerical Scheme

As the flow, heat transfer, and structure of the wedge-shaped models are simulated in COMSOL Multiphysics, the tetrahedron-shaped and prism-shaped grids are generated to discretize the fluid and solid domains. The grid systems of the pin fin and Diamond-sheet structures are shown in Figure 4. The prism-shaped boundary layer grids are finely created at all no-slip boundaries. The number of boundary layers is five, and the boundary layer stretching factor is 1.2. The thickness of the first layer is automatically selected by default with an adjustment factor of 2.5 [19,20].
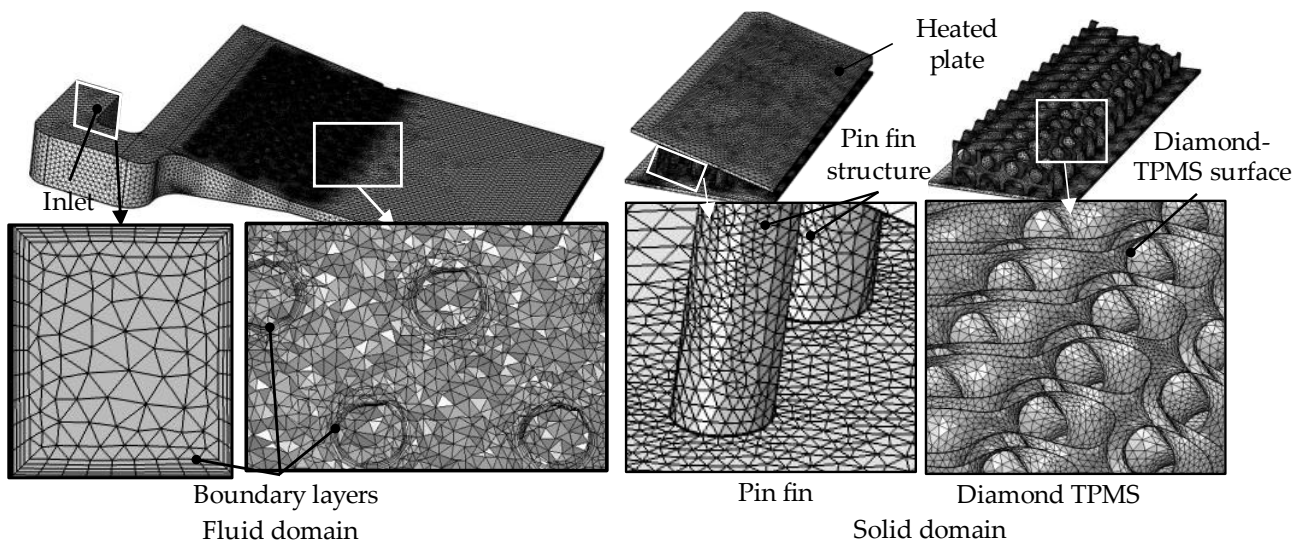
Figure 4. Representative meshes in the fluid and solid domains.

The complex flow has been observed in the cooling channel due to the pin fin structure disturbing the fluid. Liang et al. [31] found compared to the SST k-ω and RSM, the realizable k-ε turbulence model showed the most reasonable agreement with the wedge-shaped experimental results. Therefore, for all simulations in this study, the realizable k-ε model with wall treatment is chosen [19–21]. By default, the wall treatment function for

the realizable *k-ε* in COMSOL Multiphysics can approximate the fluid flow in the buffer region, significantly reducing the computational cost. Hence, the wall distance in viscous units (y^+) on most walls is limited to around 11, reaching the computational accuracy for the COMSOL requirement.

2.6. Grid Independence Check

Three grid systems (coarse, medium, and fine) with the element numbers 1.06, 1.35, and 1.80×10^6 are generated for the baseline pin fin structure to examine the grid dependence. The Nusselt number (*Nu*) from these different grid systems is plotted to test the grid independence in Figure 5. The local Nusselt number (*Nu*) in the numerical simulations is calculated as follows:

$$Nu = \frac{hD_h}{k_f} \tag{16}$$

where *h* is the local heat transfer coefficient, which is evaluated by the local wall heat flux and temperature differences between the heated wall and the corresponding bulk fluid [19–21].
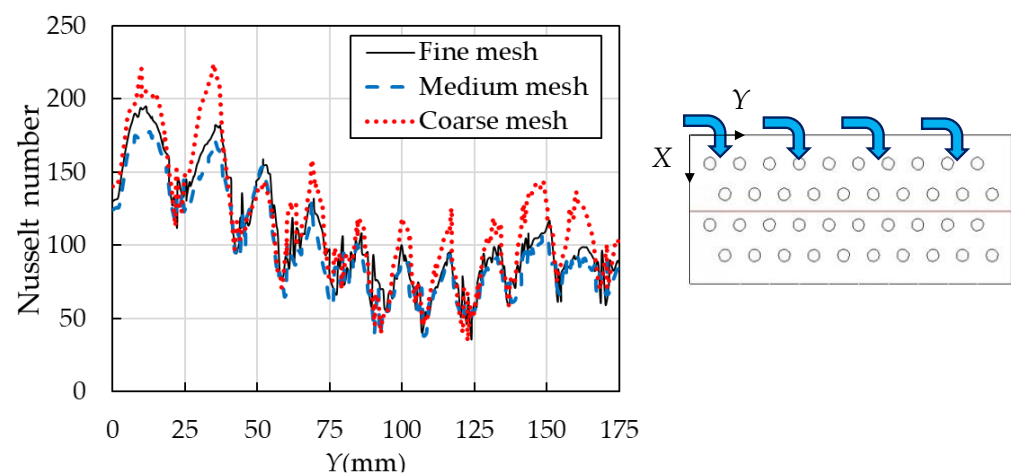
Figure 5. Nusselt number distribution on the mid-plane along the radial direction observed from different grid numbers of the baseline pin fin model at *Re* = 30,000.

The results show the Nusselt number values for all mesh systems exhibit similar trends, which decrease along the radial direction. However, coarse mesh values significantly differ from the medium and fine mesh systems. Meanwhile, the maximum deviation between the medium and fine mesh systems is negligible.

The grid convergence index method (GCI) was also employed in this numerical investigation, which has been used to report the uncertainty because of the discretization in many complex flow studies. The procedure can be surveyed in [32]. Figure 6 presents the GCI value using the spanwise-averaged Nusselt number on the endwall of the fluid domain. The line represents the finest mesh solutions, while the red bars signify the discretization errors. The maximum error is 2.4% at *Y* = 75 mm due to the large flow and temperature differences in the different mesh systems, whereas the mean error value is less than 1.0%. The grid number of 1.80×10^6 is adopted in the baseline pin fin structure, ensuring numerical accuracy. For the Diamond model, the grid system is created with setups similar to those in the baseline pin fin structure.
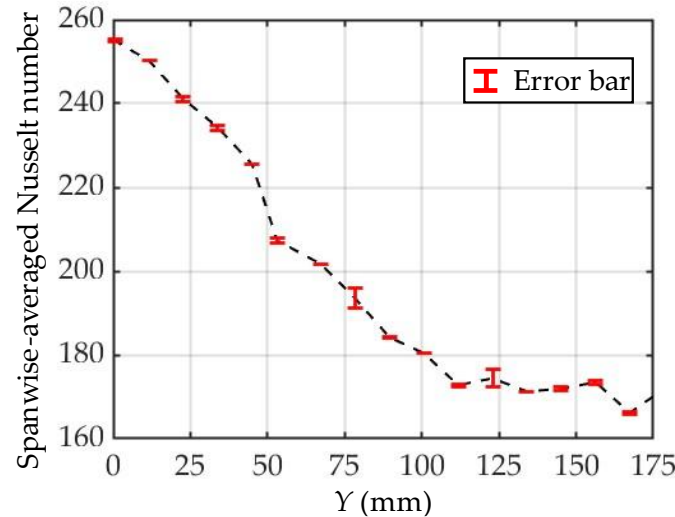
2.7. Validation

The total Nusselt number (Nu_{total}) from the experimental study by Liang et al. [26] is adopted to validate the numerical model. The total Nusselt number can be calculated as follows:

$$Nu_{total} = Nu_{avg}\left(\frac{A_{wet}}{A_{heat}}\right) \tag{17}$$

where Nu_{avg} is the area-averaged local Nusselt number. A_{wet} is the total wetted area, and A_{heat} is the projected area [26].

Figure 6. Grid convergence index values for the spanwise-averaged Nusselt number on the endwall in the radial direction observed from different grid numbers in the baseline pin fin at *Re* = 30,000.

Figure 7 shows the Nu_{total} of the numerical results is lower than the experiments for both room and high temperatures. Here, the room-temperature condition represents the model calculated with the same experimental condition using the steady-state copper plate technique with a maximum temperature of around 323.15 K by Liang et al. [26]. The results show the maximum error deviates by about 13.6%, while the mean discrepancy is 8.5% for the room-temperature condition. Meanwhile, the error for the high-temperature condition is around 25–31.8%, compared to the experimental results. These high values are because the copper material provides superior thermo-physical properties than the nickel-based alloy, causing a difference in the heat transfer [19]. However, the overall trends of the present simulation are similar to that of the room-temperature condition.
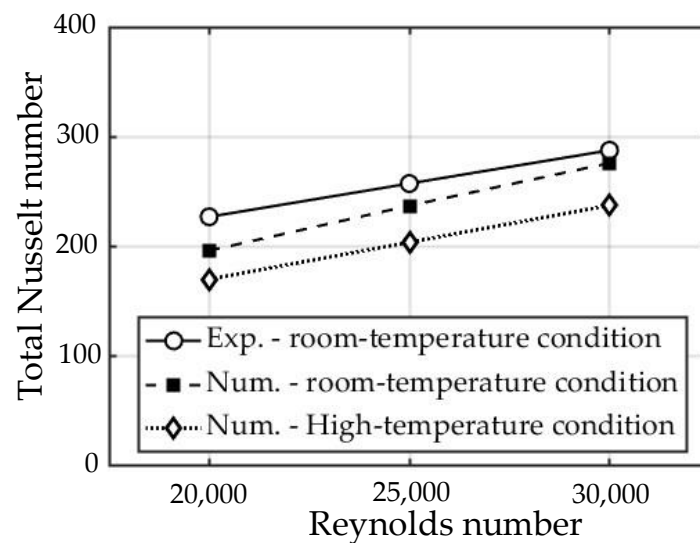
Figure 7. Model validations with experimental wedge-shaped model by Liang et al. [26].

3. Results and Discussion

This section discusses the flow, heat transfer, and structure results of the baseline pin fin and Diamond models, calculated under the high-temperature condition at *Re* = 30,000. The flow and heat transfer results of different TPMS-based structures, including the Gyroid, Diamond, and I-graph and wrapped package (IWP), at the room-temperature condition, can be observed in Ref. [20].

3.1. Flow Structures

3.1.1. Overall Flow Characteristics

The plot of 3D velocity streamlines for (a) the baseline pin fin structure and (b) the Diamond model at *Re* = 30,000 is demonstrated in Figure 8. The main coolant rushes toward the channel outlet, causing low-velocity recirculation flow at the inner wall and from the middle to the tip region for the baseline pin fin structure, as seen in Figure 8a. The impingement flow can be observed in the front of the pin elements, while the wake flow, causing a low heat transfer region, is generated behind pin fins [26].
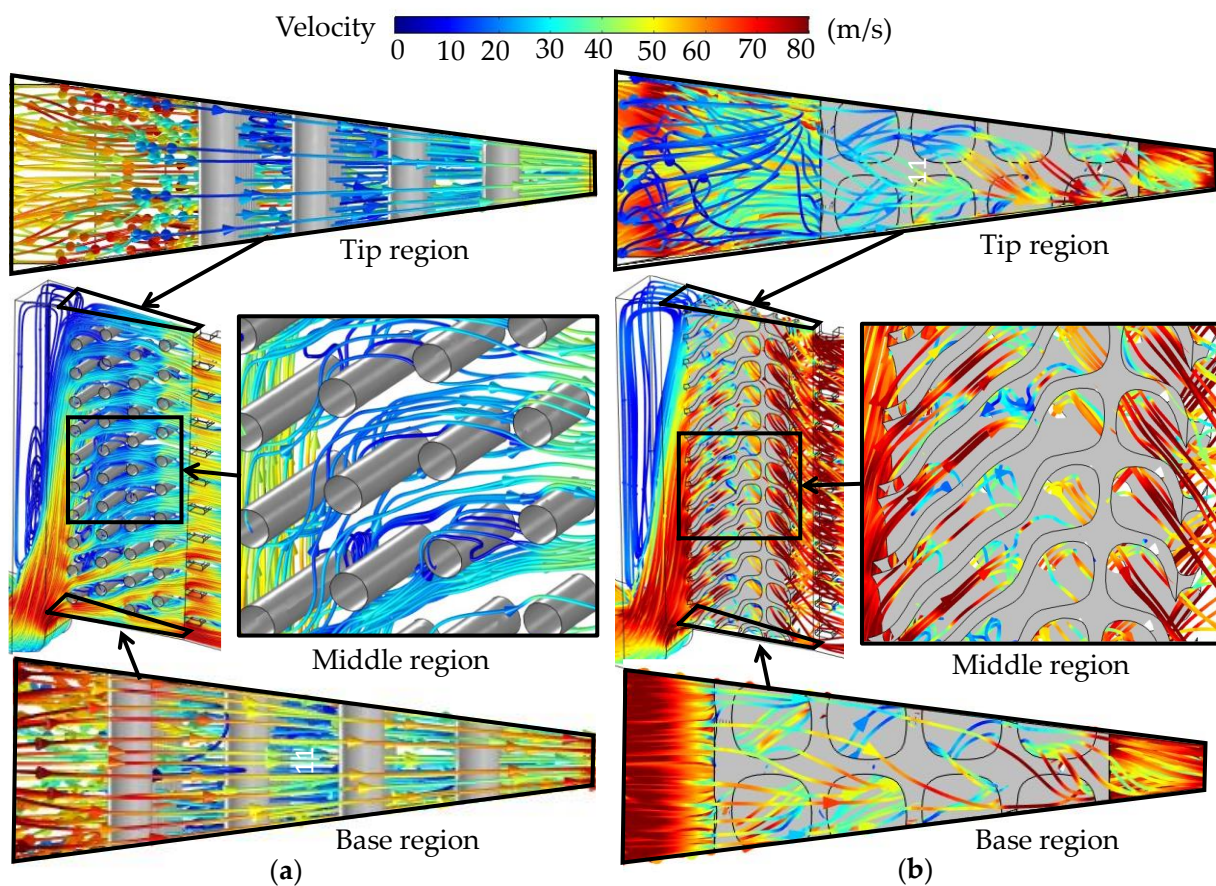

Figure 8. Overall flow structure characterized by the velocity streamlines for (**a**) baseline pin fin structure and (**b**) Diamond model at *Re* = 30,000.

Besides, the Diamond model generates a more complex flow than the circular pin fin structure, as seen in Figure 8b. The interconnected-curved walls push the coolant to the tip region; hence, the flow field is more uniform from the base to the tip region. The impingement flow is also created near the endwall due to the Diamond topology. The intensive mixing flow can be seen throughout the channel, particularly at the outlet. Overall, the flow phenomena in the Diamond model provide better flow uniformity than the baseline pin fin structure [20].

3.1.2. Turbulent Kinetic Energy Contours

The mixing features can be observed by plotting the turbulent kinetic energy distribution in the channel. Here, the contour of dimensionless turbulent kinetic energy (TKE/U_{in}^2) and surface streamlines in the middle of the channel (*X-Y* plane) for (a) the baseline pin fin structure and (b) the Diamond model at *Re* = 30,000 is presented in Figure 9. The pin fin structure provides high turbulent kinetic energy near the base region due to strong impingement flow on the first and second rows of the pin fin array. However, as the main flow is oriented toward the lateral direction, the mixing flow drastically decreases from the middle to the tip region. Meanwhile, the Diamond network induces strong mixing flow in their curved walls, increasing the turbulence, as shown in Figure 9b. The large region of high turbulent kinetic energy can be observed at the channel outlet because of the flow contraction in the narrow region of the wedge-shaped channel [19,20]. The more intensive turbulence in the Diamond model provides higher heat transfer than in the baseline pin fin structure.

(a) **(b)**
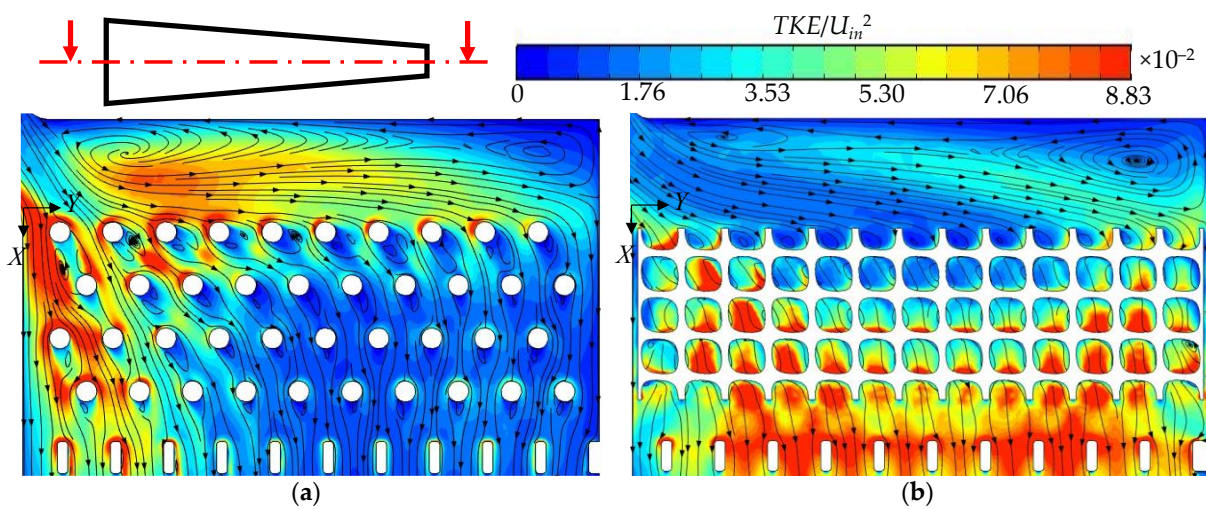
Figure 9. Dimensionless turbulent kinetic energy and surface streamlines in the middle of the channel (*X-Y* plane) for (**a**) baseline pin fin structure and (**b**) Diamond model at *Re* = 30,000.

3.1.3. Relative Pressure Coefficient Distributions

The relative pressure coefficient calculated based on local pressure at the measuring region (p_{loc}) is used to characterize the pressure loss. It can be calculated as follows:

$$C_p = \frac{p_{loc} - p_{ref}}{\rho U_{loc}^2 / 2} \tag{18}$$

where p_{ref} is the reference pressure measured at the inlet boundary, and U_{loc} is the local velocity.

Figure 10 demonstrates the contour of the relative pressure coefficient along with the surface streamlines in the middle of the channel (*X-Y* plane) for (a) the baseline pin fin structure and (b) the Diamond model at *Re* = 30,000. Both models cause large areas of low-pressure coefficient values at the inner wall because of changes in the flow direction. For the baseline pin fin structure, the wake flow behind the pin elements causes a low-pressure coefficient value, as seen in Figure 10a. Besides, the Diamond model provides a uniform distribution of the relative pressure coefficient in its network. The values at the channel outlet are also lower than in the baseline pin fin case because the flow is contracted in the Diamond model, accelerating the high velocity. However, the volume average of the relative pressure coefficient in the Diamond model is 45.9% higher than in the baseline pin fin structure. The total pressure, calculated from the pressure difference between the inlet and outlet, in the Diamond model is higher than the pin fin structure by 201%.
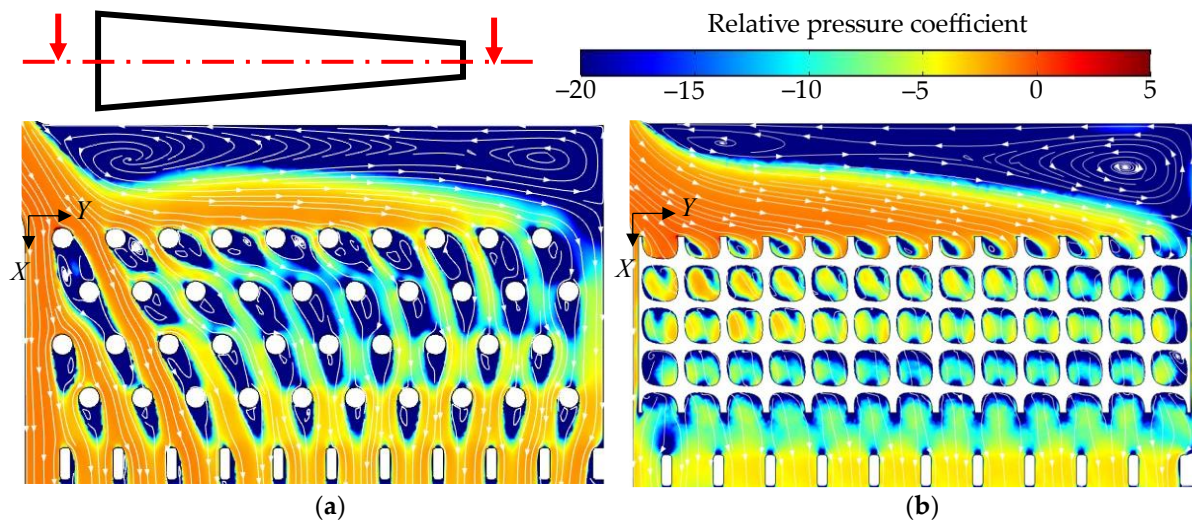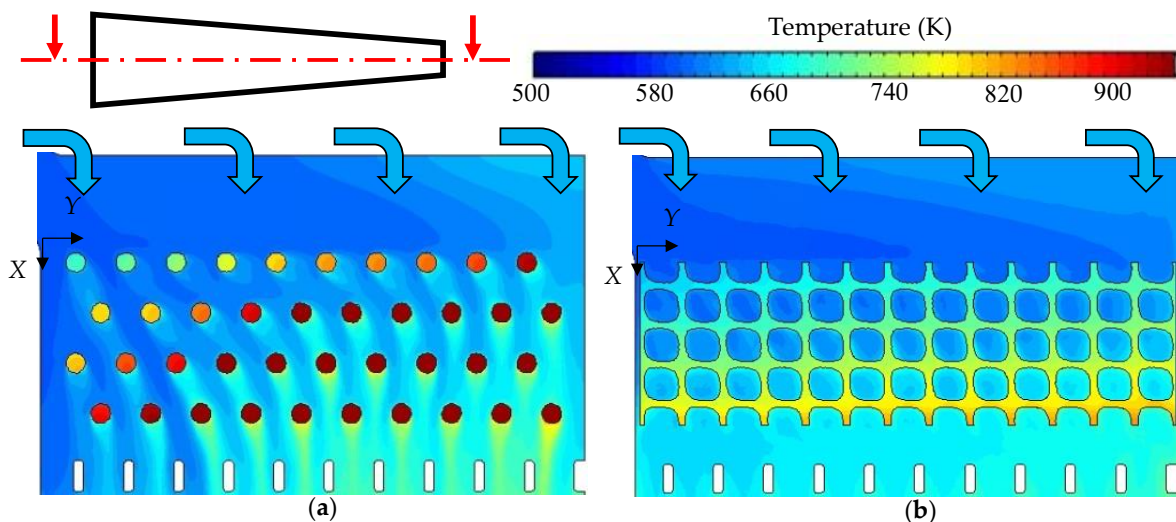
Figure 10. Relative pressure loss distribution and surface streamline in the middle of the channel (*X-Y* plane) for (**a**) baseline pin fin structure and (**b**) Diamond model at *Re* = 30,000.

3.2. Heat Transfer

3.2.1. Temperature Distributions

The temperature distribution in the fluid and solid domains in the middle of the channel (*X-Y* plane) is demonstrated in Figure 11. In the fluid domain, the low-temperature region at the inner wall in the baseline pin fin structure is larger than in the Diamond model because the low-temperature coolant mainly leaves the channel near the base region, causing less contact between the hot structure and cool flow. Hence, the pin fin elements remain at higher temperatures than the Diamond structure, particularly the pin near the tip region. Moreover, it is evident the Diamond model generates more uniform temperature distribution for both solid and fluid domains.

Figure 11. Temperature distribution in the middle of the channel (*X-Y* plane), including fluid and solid domains for (**a**) baseline pin fin structure and (**b**) Diamond model at *Re* = 30,000.
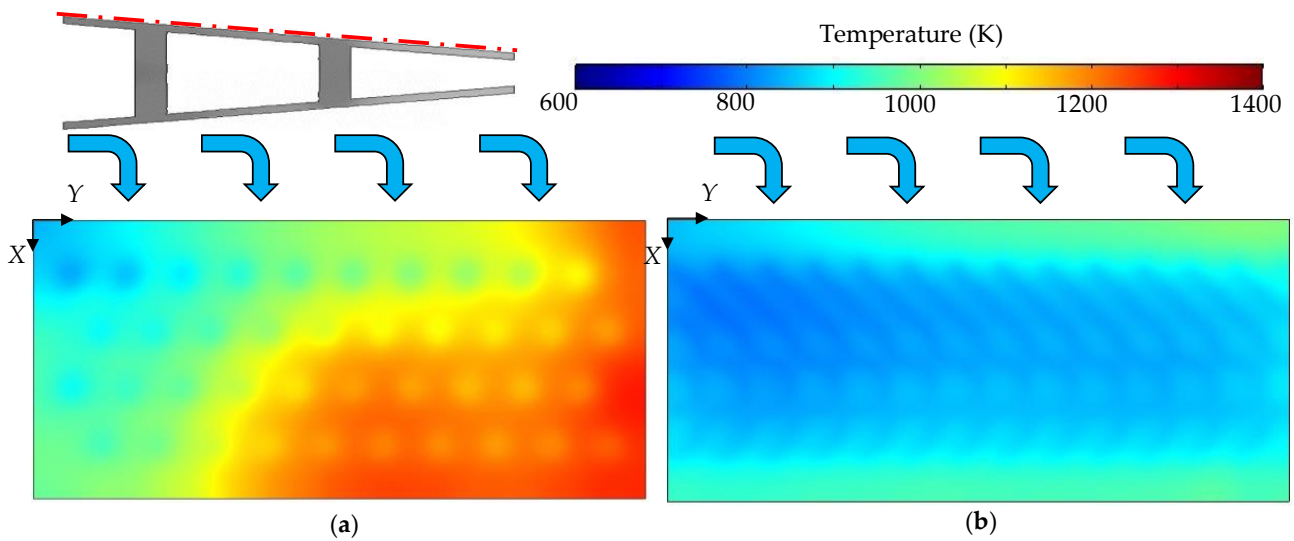
The temperature distribution in the solid domain from different *Z-X* cross-sections for (a) the baseline pin fin structure and (b) the Diamond model at *Re* = 30,000 is presented in Figure 12. The Diamond model causes lower temperatures than the baseline pin fin structure because the large, wetted areas of the Diamond curved walls exchange the heat better. The temperature distributions in the Diamond network are also uniform, reducing the thermal stress concentration due to high-temperature differences.
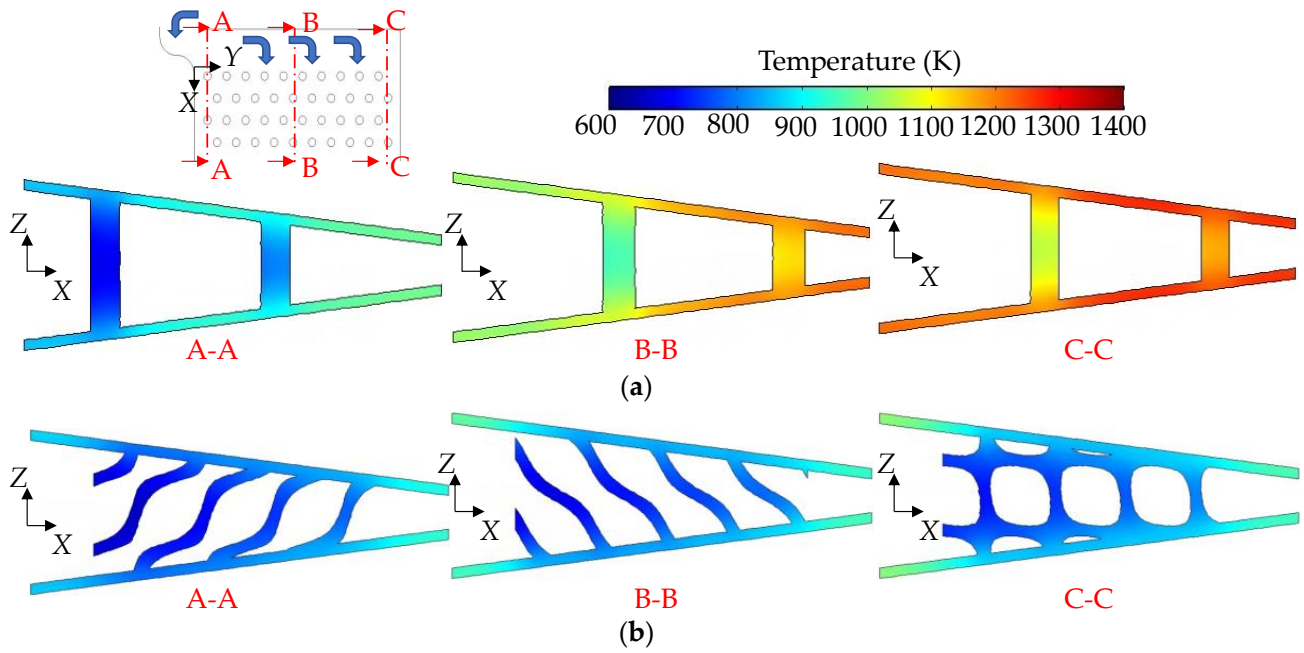
Figure 12. Temperature distribution in different *Z-X* cross-sections of the solid domain for (**a**) baseline pin fin structure and (**b**) Diamond model at *Re* = 30,000.

Furthermore, to observe the temperature gains from the hot flow mainstream, the temperature distribution on the external wall of the solid domain for (a) the baseline pin fin structure and (b) the Diamond model at *Re* = 30,000 is presented in Figure 13. It can be clearly seen the temperature in the Diamond model is much lower than in the baseline pin fin structure. The average temperature on the external wall in the Diamond model is reduced by 19.9% compared to the baseline pin fin structure. The low-temperature regions are attributed to the complex flow generated in the Diamond curved walls. Moreover, the temperature distributions in the Diamond model are much more uniform than in the baseline pin fin structure, mitigating the thermal failure of gas turbine blades under high operating temperature conditions.

Figure 13. Temperature distribution on the external surface of the solid domain for (**a**) baseline pin fin structure and (**b**) Diamond model at *Re* = 30,000.

3.2.2. Overall Thermal Performance

The thermal performance of cooling channels is used to assess the heat transfer performance after evaluating the flow resistance in the channel. In this investigation, the thermal performance enhancement (*TPF*) is presented, which can be calculated as follows:

$$TPF = \frac{Nu_{total}/Nu_0}{(f/f_0)^{1/3}}$$

(19)

where Nu_0 and f_0 are the Dittus–Boelter ($Nu_0 = 0.023Re^{0.8}Pr^{0.4}$) and Blasius equations ($f_0 = 0.316Re^{-0.25}$), respectively. *Pr* is the Prandtl number of air, fixed at *Pr* = 0.7. *f* is the friction factor, defined as follows:

$$f = \frac{2\Delta p D_h}{\rho U_{in}^2 L_c}$$

(20)

where Δp is the total pressure loss calculated by $\Delta p = p_{in} - p_{out}$; p_{in} and p_{out} are the inlet and outlet pressures.

Figure 14 compares the total Nusselt number ratio, friction factor ratio, and thermal performance enhancement of the baseline pin fin and Diamond structures at the *Re* = 30,000. The results show the Diamond model offers a much higher total Nusselt number ratio than the baseline pin fin structure due mainly to larger wetted areas of the Diamond topology. The total Nusselt number ratio is 145.3%, superior to the baseline pin fin structure, as seen in Figure 14a.
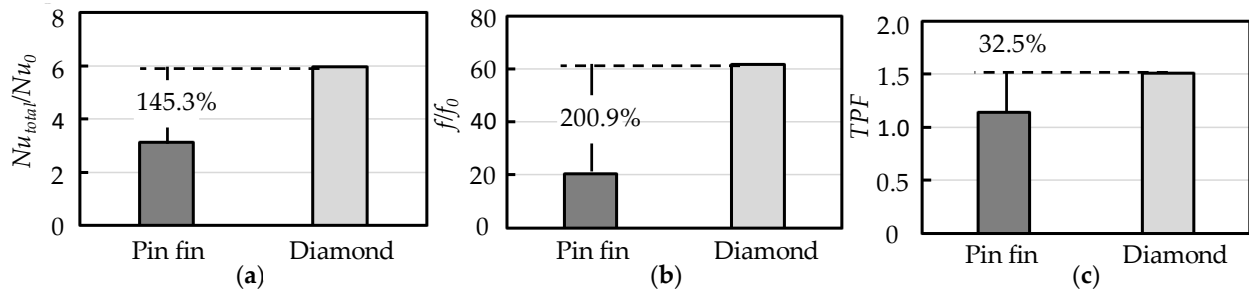

Figure 14. Comparisons of (**a**) total Nusselt number ratio, (**b**) friction factor ratio, and (**c**) thermal performance enhancement for the baseline pin fin structure and Diamond model at *Re* = 30,000.

Since the interconnected-curved walls of the Diamond model significantly increase the flow resistance in the channel, the friction factor value of the Diamond model is higher than that of the baseline pin fin structure by about 200.9%, as shown in Figure 14b. Moreover, the high friction value can be attributed to the combined effect between the wedged shape and the large Diamond-TPMS volume in the channel. However, the thermal performance enhancement of the Diamond model is increased by 32.5% compared to the baseline pin fin structure, as presented in Figure 14c. It is observed the increase in the thermal performance enhancement in this study is lower than in the previous investigation by Yeranee and Rao [20] because the thermal conductivity of the alloy is much lower than in the copper; hence, the heat transfer between the hot surface and coolant is deficient [19].
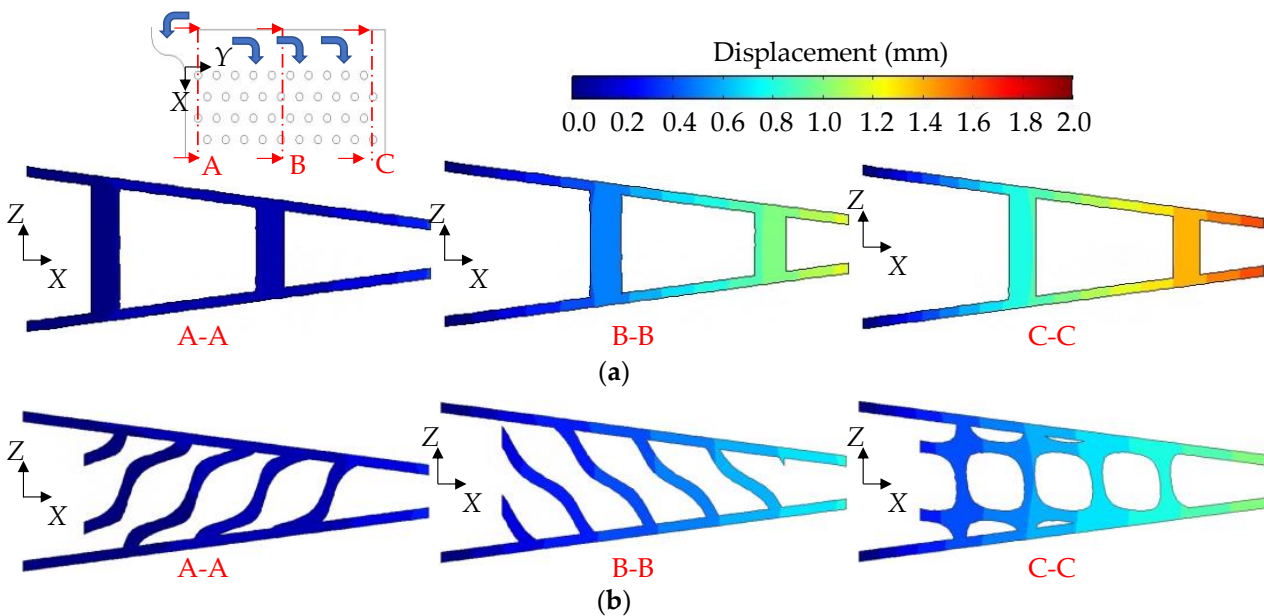
3.3. Displacement

The displacement contour on the channel between the baseline pin fin and Diamond structures is demonstrated in Figure 15. The results of high temperature deform the blade because of thermal expansion. For both structures, the largest deformation is observed at the tip region near the channel outlet [30]. The maximum displacement in the baseline pin fin structure is 1.74 mm, while in the Diamond, the maximum value is 1.12 mm. The Diamond structure in the wedge-shaped channel helps reduce the volume displacement due to the material thermal expansion by about 29.3%, as compared to the baseline model. Furthermore, as the ceramic material can be used to additively manufacture complex

structures via the PBF [2] in the future, the displacement and temperature distribution of the gas turbine blade can be further improved [3–5].
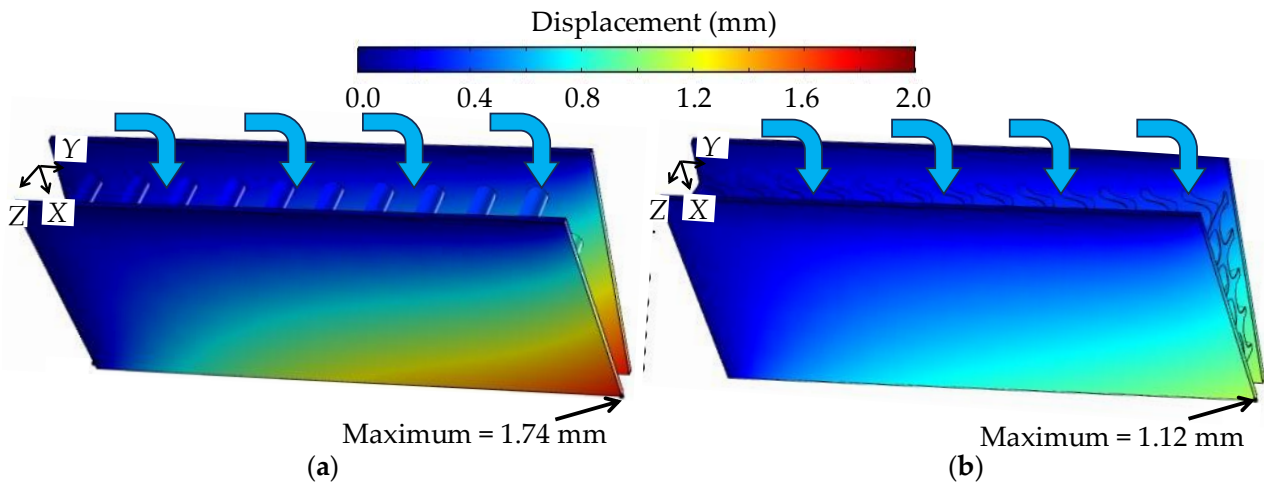
Figure 15. Displacement distribution for (**a**) baseline pin fin structure and (**b**) Diamond model at *Re* = 30,000.

Figure 16 compares the displacement contour at *Z-X* different cross-sections on the wedge-shaped solid domain between the baseline pin fin and Diamond structures. Both cases cause a large displacement near the tip region. Due to the high-temperature gradient, the displacement also emerges in the pin fin elements and Diamond structures. Nonetheless, the displacement in the Diamond model is smaller and evenly distributed, as seen in plane C-C of Figure 16b. The uniform deformation in the Diamond model could reduce the sudden cracks on the trailing edge gas turbine blade.


Figure 16. Displacement distribution along the radial direction plane for (**a**) baseline pin fin structure and (**b**) Diamond model at *Re* = 30,000.
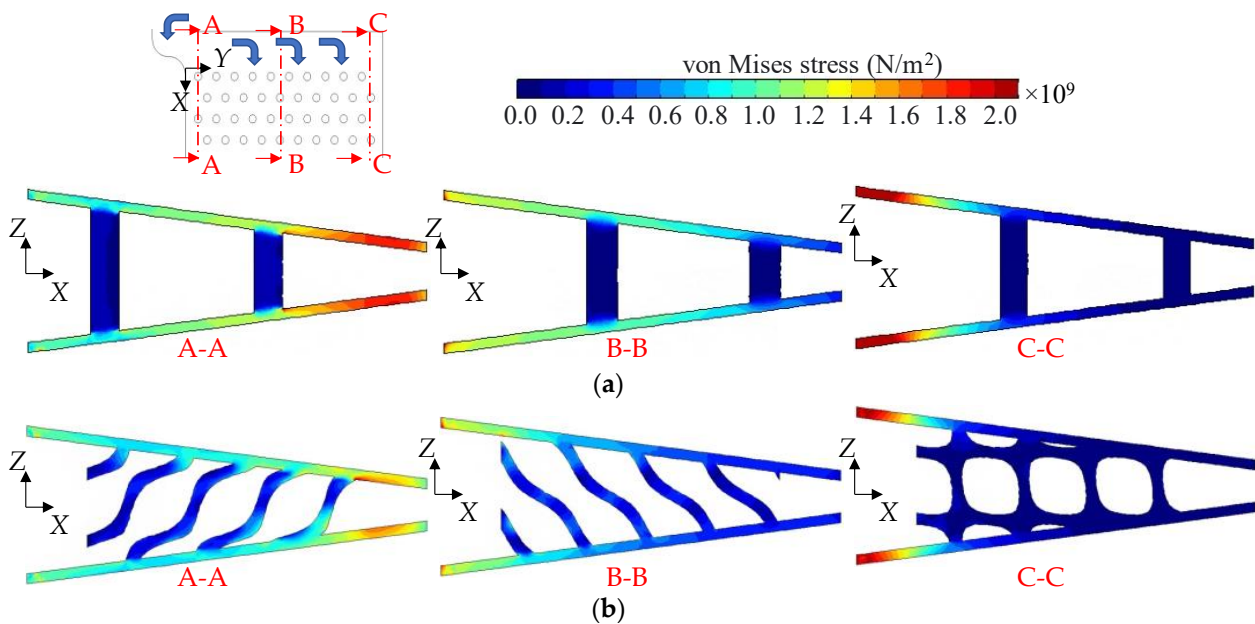
3.4. Thermal Stress

Figure 17 shows the contour of von Mises stress on the top plate for the baseline pin fin and Diamond models at *Re* = 30,000. Both cases expose similar stress patterns, where the highest stresses emerge at the fixed boundaries due to high-temperature differences

between the fluid and solid domains, as seen in Figure 13. Here, the Diamond model causes smaller areas of high stress than the baseline pin fin structure. Also, the von Mises stress in the Diamond structure is distributed more evenly because of the interconnected network in the channel. The volume average of von Mises stress in the Diamond structure is reduced by 28.8% compared to that in the baseline pin fin model.
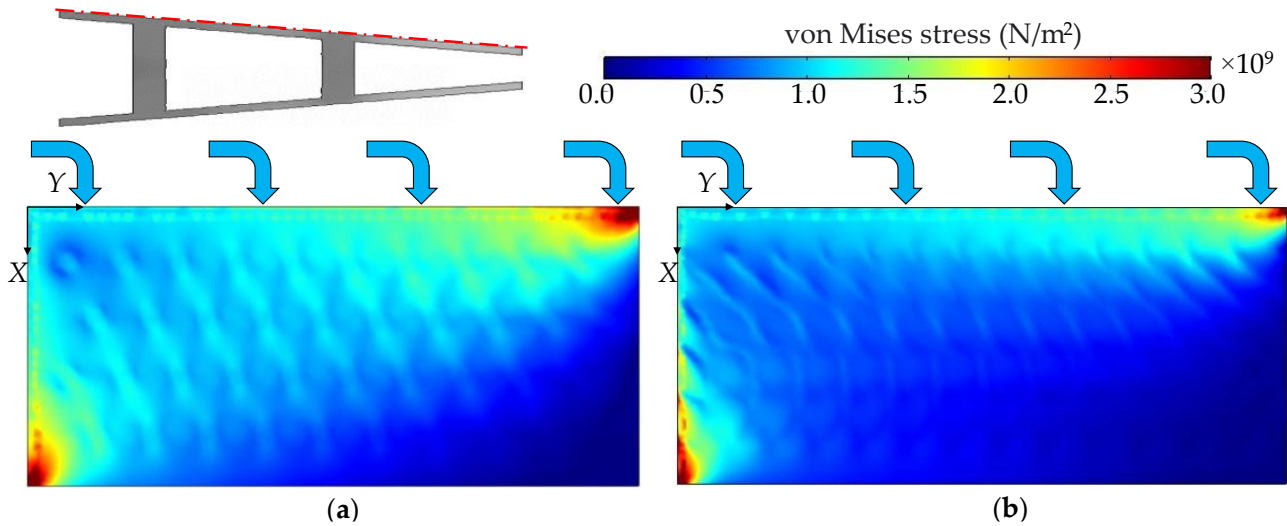
Figure 17. Thermal stress distribution on the external surface of the solid domain for (**a**) baseline pin fin structure and (**b**) Diamond model at *Re* = 30,000.

The comparison of von Mises stress distribution at the different *Z-X* cross-sections between the baseline pin fin and Diamond models at *Re* = 30,000 is shown in Figure 18. For the baseline pin fin structure, the areas of high stress are found on the plates, while for the Diamond model, the region of medium stress can also be observed on the Diamond curved walls. As the stress distributes on the Diamond networks, the thermal stress on the plates of the Diamond model is lower than that of the baseline pin fin model. This result significantly mitigates the thermal failure of the trailing edge gas turbine blade.

Figure 18. Thermal stress distribution along the radial direction plane for (**a**) baseline pin fin structure and (**b**) Diamond model at *Re* = 30,000.

4. Conclusions

This study aims to demonstrate the turbulent flow heat transfer and thermal stress of the optimal TPMS-based structure (Diamond topology) in the gas turbine blade trailing cooling channel. The thermal-fluid-solid analysis of the Diamond model at the nearly realistic gas turbine condition is executed, and the results are compared with the conventional pin fin structure at $Re = 30,000$. Flow characteristics, heat transfer performance, temperature distribution, displacement, and thermal stress of the Diamond model are discussed and compared with the baseline pin fin structure. Based on the analysis, the conclusions are shown as follows:

1. The Diamond model distributes fluid more evenly throughout the channel than the baseline pin fin structure. The recirculation flow at the inner wall and in the channel is significantly reduced due to the interconnected-curved walls of the Diamond network. The overall heat transfer enhancement, friction factor ratio, and thermal performance in the Diamond model are increased by 145.3%, 200.9%, and 32.5%, respectively, compared to the baseline pin fin structure.

2. The lower fluid temperatures occur at the tip region and the heating zone when inserting the Diamond structure in the wedge-shaped channel. A better temperature uniformity can also be noticeable, especially at the channel outlet. Moreover, the Diamond structure shows a uniform temperature on the surface and causes lower temperatures than the baseline pin fin model. The average temperature on the top plate in the Diamond case reduces by 19.9% compared to that of the baseline pin fin structure.

3. The largest deformation is observed at the tip outlet for both cases. The Diamond model in the wedge-shaped channel helps reduce the volume displacement as a result of the material thermal expansion by about 29.3% compared to the baseline pin fin structure. Also, the displacement in the Diamond model is smaller and evenly distributed. The uniform deformation in the Diamond model could reduce the sudden cracks on the trailing edge gas turbine blade.

4. The Diamond model causes smaller areas of high stress than the baseline pin fin structure. Also, the von Mises stress in the Diamond structure is more uniform because the high temperature is distributed through the interconnected network. The volume average of von Mises stress in the Diamond structure reduces by 28.8% compared to that in the baseline pin fin structure.

Overall, the Diamond model shows better flow, heat transfer, and mechanical performances in the trailing edge than the conventional pin fin array. Different TPMS topologies could be combined to obtain better thermal and mechanical performances. Optimization is also the preferred method to optimize the thickness and cell size of the TPMS structures. In the future, as the ceramic material is being developed to additively manufacture TPMS-based structures via the PBF, the displacement and temperature distribution of the gas turbine blade can be further improved; hence, the thermal stress is significantly reduced, mitigating the failure of gas turbine blades.

References

1. Perepezko, J.H. The Hotter the Engine, the Better. *Science* **2009**, *326*, 1068–1069. [CrossRef] [PubMed]
2. Grossin, D.; Montón, A.; Navarrete-Segado, P.; Özmen, E.; Urruth, G.; Maury, F.; Maury, D.; Frances, C.; Tourbin, M.; Lenormand, P.; et al. A Review of Additive Manufacturing of Ceramics by Powder Bed Selective Laser Processing (Sintering/Melting): Calcium Phosphate, Silicon Carbide, Zirconia, Alumina, and Their Composites. *Open Ceram.* **2021**, *5*, 100073. [CrossRef]
3. Nekahi, S.; Vaferi, K.; Vajdi, M.; Sadegh Moghanlou, F.; Shahedi Asl, M.; Shokouhimehr, M. A Numerical Approach to the Heat Transfer and Thermal Stress in a Gas Turbine Stator Blade Made of HfB2. *Ceram. Int.* **2019**, *45*, 24060–24069. [CrossRef]
4. Sadegh Moghanlou, F.; Vajdi, M.; Motallebzadeh, A.; Sha, J.; Shokouhimehr, M.; Shahedi Asl, M. Numerical Analyses of Heat Transfer and Thermal Stress in a ZrB2 Gas Turbine Stator Blade. *Ceram. Int.* **2019**, *45*, 17742–17750. [CrossRef]
5. Abid, A.; Sarowar, M.T. Heat Transfer, Thermal Stress and Failure Inspection of a Gas Turbine Compressor Stator Blade Made of Five Different Conventional Superalloys and Ultra-High-Temperature Ceramic Material: A Direct Numerical Investigation. *J. Fail. Anal. Prev.* **2022**, *22*, 878–898. [CrossRef]
6. Han, J.-C.; Dutta, S.; Ekkad, S. *Gas Turbine Heat Transfer and Cooling Technology*, 2nd ed.; CRC Press: Boca Raton, FL, USA, 2012; ISBN 9780429107115.
7. Li, L.; Liu, C.; Liu, H.; Zhu, H.; Luo, J. Investigation on Film Cooling Performance of the Compound Hole and Y-Shaped Hole Configurations with the Cross-Flow Coolant Channel. In Proceedings of the Volume 5C: Heat Transfer, Oslo, Norway, 11 June 2018; pp. 1–14.
8. Yeranee, K.; Rao, Y. A Review of Recent Studies on Rotating Internal Cooling for Gas Turbine Blades. *Chin. J. Aeronaut.* **2021**, *34*, 85–113. [CrossRef]
9. Du, W.; Luo, L.; Jiao, Y.; Wang, S.; Li, X.; Sunden, B. Heat Transfer in the Trailing Region of Gas Turbines—A State-of-the-Art Review. *Appl. Therm. Eng.* **2021**, *199*, 117614. [CrossRef]
10. Xi, L.; Gao, J.; Xu, L.; Zhao, Z.; Yang, T.; Li, Y. Study on Flow and Heat Transfer Performance of a Rectangular Channel Filled with X-Shaped Truss Array under Operating Conditions of Gas Turbine Blades. *Aerospace* **2022**, *9*, 533. [CrossRef]
11. Xi, L.; Gao, J.; Xu, L.; Zhao, Z.; Yang, Z.; Li, Y. Numerical Investigation on Cooling Performance of Rectangular Channels Filled with X-Shaped Truss Array Structures. *Aerospace* **2022**, *9*, 405. [CrossRef]
12. Kaur, I.; Singh, P. Endwall Heat Transfer Characteristics of Octahedron Family Lattice-Frame Materials. *Int. Commun. Heat Mass Transf.* **2021**, *127*, 105522. [CrossRef]
13. Kaur, I.; Aider, Y.; Nithyanandam, K.; Singh, P. Thermal-Hydraulic Performance of Additively Manufactured Lattices for Gas Turbine Blade Trailing Edge Cooling. *Appl. Therm. Eng.* **2022**, *211*, 118461. [CrossRef]
14. Shen, B.; Li, Y.; Yan, H.; Boetcher, S.K.S.; Xie, G. Heat Transfer Enhancement of Wedge-Shaped Channels by Replacing Pin Fins with Kagome Lattice Structures. *Int. J. Heat Mass Transf.* **2019**, *141*, 88–101. [CrossRef]
15. Yeranee, K.; Rao, Y. A Review of Recent Investigations on Flow and Heat Transfer Enhancement in Cooling Channels Embedded with Triply Periodic Minimal Surfaces (TPMS). *Energies* **2022**, *15*, 8994. [CrossRef]
16. Kaur, I.; Singh, P. Flow and Thermal Transport Characteristics of Triply-Periodic Minimal Surface (TPMS)-Based Gyroid and Schwarz-P Cellular Materials. *Numer. Heat Transf. Part A Appl.* **2021**, *79*, 553–569. [CrossRef]
17. Khalil, M.; Hassan Ali, M.I.; Khan, K.A.; Abu Al-Rub, R. Forced Convection Heat Transfer in Heat Sinks with Topologies Based on Triply Periodic Minimal Surfaces. *Case Stud. Therm. Eng.* **2022**, *38*, 102313. [CrossRef]
18. Yinzheng, Z. Numerical Analysis On Fluid-Solid Coupling Cooling Of Minimal Surface Lattice Structure. *J. Phys. Conf. Ser.* **2019**, *1187*, 032070. [CrossRef]
19. Yeranee, K.; Rao, Y. Turbulent Flow and Heat Transfer Enhancement for Turbine Blade Trailing Edge Cooling with Gyroid-Type Triply Periodic Minimal Surfaces. *J. Eng. Gas Turbines Power* **2023**, *145*, 071008. [CrossRef]
20. Yeranee, K.; Rao, Y. Heat Transfer and Pressure Loss of Turbulent Flow in a Wedge-Shaped Cooling Channel with Different Types of Triply Periodic Minimal Surfaces. *ASME J. Heat Mass Transf.* **2023**, *145*, 093901. [CrossRef]
21. Yeranee, K.; Rao, Y.; Xu, C.; Chen, J. Rotating Effects on Flow and Heat Transfer Characteristics in a Wedge-Shaped Cooling Channel with Diamond Structure Based on Triply Periodic Minimal Surfaces. In Proceedings of the International Gas Turbine Congress, Kyoto, Japan, 26 November–1 December 2023; pp. 3–6.
22. Alkebsi, E.A.A.; Ameddah, H.; Outtas, T.; Almutawakel, A. Design of Graded Lattice Structures in Turbine Blades Using Topology Optimization. *Int. J. Comput. Integr. Manuf.* **2021**, *34*, 370–384. [CrossRef]
23. Timercan, A.; Sheremetyev, V.; Brailovski, V. Mechanical Properties and Fluid Permeability of Gyroid and Diamond Lattice Structures for Intervertebral Devices: Functional Requirements and Comparative Analysis. *Sci. Technol. Adv. Mater.* **2021**, *22*, 285–300. [CrossRef]
24. Laskowska, D.; Szatkiewicz, T.; Bałasz, B.; Mitura, K. Mechanical Properties and Energy Absorption Abilities of Diamond TPMS Cylindrical Structures Fabricated by Selective Laser Melting with 316L Stainless Steel. *Materials* **2023**, *16*, 3196. [CrossRef] [PubMed]
25. Timercan, A.; Terriault, P.; Brailovski, V. Axial Tension/Compression and Torsional Loading of Diamond and Gyroid Lattice Structures for Biomedical Implants: Simulation and Experiment. *Mater. Des.* **2023**, *225*, 111585. [CrossRef]
26. Liang, C.; Rao, Y.; Chen, J.; Zhang, P. Experimental and Numerical Study of the Turbulent Flow and Heat Transfer in a Wedge-Shaped Channel With Guiding Pin Fin Arrays Under Rotating Conditions. *J. Turbomach.* **2022**, *144*, 071007. [CrossRef]
27. Al-Ketan, O.; Abu Al-Rub, R.K. MSLattice: A Free Software for Generating Uniform and Graded Lattices Based on Triply Periodic Minimal Surfaces. *Mater. Des. Process. Commun.* **2021**, *3*, e205. [CrossRef]

28. Pierce, A.D.; Beyer, R.T. Acoustics: An Introduction to Its Physical Principles and Applications. 1989 Edition. *J. Acoust. Soc. Am.* **1990**, *87*, 1826–1827. [CrossRef]

29. Boyce, M.P. Materials. In *Gas Turbine Engineering Handbook*; Boyce, M.P., Ed.; Elsevier: Oxford, UK, 2012; pp. 493–514, ISBN 978-0-12-383842-1.

30. Ikpe, A.; Efe-Ononeme, O.; Ariavie, G. Thermo-Structural Analysis of First Stage Gas Turbine Rotor Blade Materials for Optimum Service Performance. *Int. J. Eng. Appl. Sci.* **2018**, *10*, 118–130. [CrossRef]

31. Liang, C.; Rao, Y.; Luo, J.; Luo, X. Experimental and Numerical Study of Turbulent Flow and Heat Transfer in a Wedge-Shaped Channel with Guiding Pin Fins for Turbine Blade Trailing Edge Cooling. *Int. J. Heat Mass Transf.* **2021**, *178*, 121590. [CrossRef]

32. Celik, I.B.; Ghia, U.; Roache, P.J.; Freitas, C.J.; Coleman, H.; Raad, P.E. Procedure for Estimation and Reporting of Uncertainty Due to Discretization in CFD Applications. *ASME J. Fluids Eng.* **2008**, *130*, 078001. [CrossRef]